Article
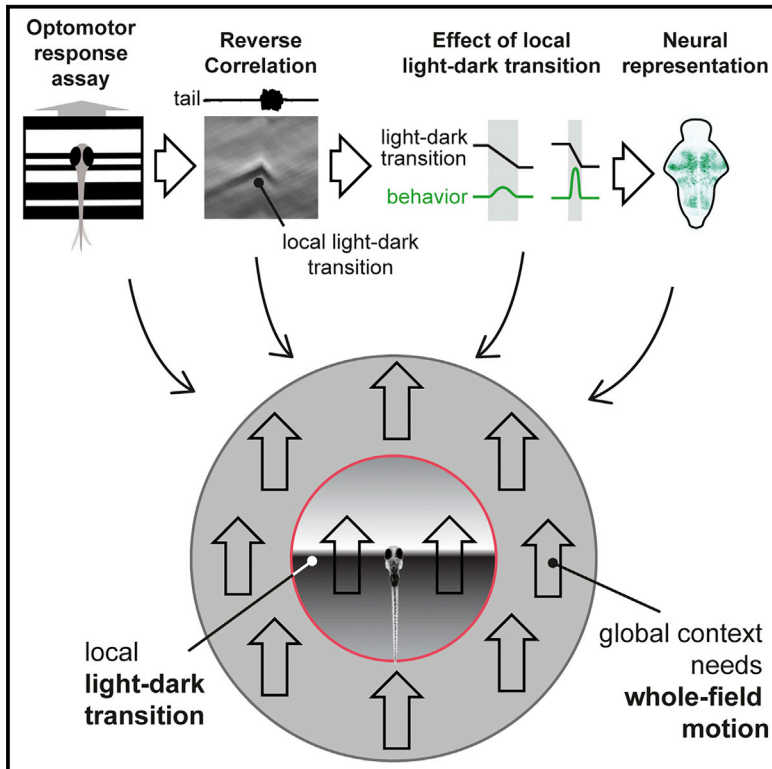
Optomotor Swimming in Larval Zebrafish Is Driven by Global Whole-Field Visual Motion and Local Light-Dark Transitions

Graphical Abstract

Authors

Andreas M. Kist, Ruben Portugues

Correspondence

rportugues@neuro.mpg.de

In Brief

Kist and Portugues use reverse correlation in an optomotor behavioral assay in larval zebrafish to identify the stereotypic filter that elicits swimming. It consists of a forward-moving local light-dark transition alongside global whole-field motion. The luminance profile strongly affects behavioral parameters, and filter-specific activity is spread across the brain.

Highlights

- Behavioral reverse correlation reveals the filter that drives optomotor swimming

- The filter consists of a forward-moving local off edge and global whole-field motion

- Light-dark transition is robustly found across both fish and stimuli parameters

- Filter-specific neural activity is found across the zebrafish brain

CellPress

Article

Optomotor Swimming in Larval Zebrafish Is Driven by Global Whole-Field Visual Motion and Local Light-Dark Transitions

Andreas M. Kist[1,2] and Ruben Portugues[1,3,*]

[1]Max Planck Institute of Neurobiology, Sensorimotor Control Research Group, Am Klopferspitz 18, 82152 Martinsried, Germany
[2]Division of Phoniatrics and Pediatric Audiology, Department of Otorhinolaryngology, Head and Neck Surgery, University Hospital Erlangen,
Friedrich-Alexander-University Erlangen-Nürnberg, Waldstr. 1, 91054 Erlangen, Germany
[3]Lead Contact
*Correspondence: rportugues@neuro.mpg.de
https://doi.org/10.1016/j.celrep.2019.09.024

SUMMARY

Stabilizing gaze and position within an environment constitutes an important task for the nervous system of many animals. The optomotor response (OMR) is a reflexive behavior, present across many species, in which animals move in the direction of perceived whole-field visual motion, therefore stabilizing themselves with respect to the visual environment. Although the OMR has been extensively used to probe visuomotor neuronal circuitry, the exact visual cues that elicit the behavior remain unidentified. In this study, we use larval zebrafish to identify spatio-temporal visual features that robustly elicit forward OMR swimming. These cues consist of a local, forward-moving, off edge together with on/off symmetric, similarly directed, global motion. Imaging experiments reveal neural units specifically activated by the forward-moving light-dark transition. We conclude that the OMR is driven not just by whole-field motion but by the interplay between global and local visual stimuli, where the latter exhibits a strong light-dark asymmetry.

INTRODUCTION

A behavior essential for survival is the ability of animals to position themselves stably in their environment. In the case of the visual environment, an often-used strategy is to move in order to cancel any relative motion between the animal and the visual motion, i.e., to minimize visual motion or retinal slip. In response to global, translational, whole-field motion, larval zebrafish will swim in the direction of perceived motion by generating swimming events called bouts. This reflex is known as the optomotor response (OMR) and can be elicited in both freely swimming and head-restrained zebrafish (Clark, 1981; Orger et al., 2000; Portugues and Engert, 2011), flies (Borst et al., 2010), mice (Matsuo et al., 2018; Shi et al., 2018), and many other species (Dieringer et al., 1982).

Under experimental conditions, the OMR has typically been elicited using simple synthetic stimuli, such as sinusoidal or square gratings (Naumann et al., 2016; Neuhauss et al., 1999;

Orger et al., 2000, 2008), and functional imaging experiments have shown that a large number of neurons throughout the brain are activated during this behavior (Ahrens et al., 2012; Kubo et al., 2014; Naumann et al., 2016; Portugues et al., 2014). Nevertheless, from a visual processing perspective, both the precise visual features that trigger this behavior and the circuitry that processes these features remain largely unknown. Behaviorally, OMR swimming has been shown to be driven by green and red cones (Orger and Baier, 2005) and Fourier and non-Fourier visual motion (Orger et al., 2000). The OMR further depend on the speed of fixed period square gratings (Portugues et al., 2015; Severi et al., 2014) and on the visual reafference perceived during swimming (Ahrens et al., 2012; Portugues and Engert, 2011). In terms of neuronal processing, despite a number of elegant studies characterizing the projection of retinal ganglion cells (RGCs) to the ten retino-recipient areas in the zebrafish brain (Burrill and Easter, 1994; Robles et al., 2014), the functional involvement of these RGC arborization fields (AFs) in the OMR remains unclear (Burgess et al., 2010; Muto et al., 2005; Nikolaou et al., 2012; Roeser and Baier, 2003; Temizer et al., 2015). In addition, several studies have signaled the pretectum as an important hub where OMR sensory drive is represented (Chen et al., 2018; Kubo et al., 2014; Naumann et al., 2016).

In this study, we investigate the precise visual features that drive OMR swimming in larval zebrafish. We extend the concept of a receptive field, as usually defined in neurophysiological recordings, to behavior to compute a behavioral receptive field. In neurophysiology, the optimal stimulus, called the spike-triggered average (STA), that makes a neuron fire can be computed using reverse correlation between the neuronal firing and the changing stimulus that was presented (DeCharms and Merzenich, 1998; Marmarelis and Marmarelis, 1978; Ringach et al., 1997; Schwartz et al., 2006; see Figure 1A). The STA can subsequently be used as a linear filter in a linear-nonlinear-Poisson (LNP) cascade model (Figure 1B) to, for example, describe firing patterns of neurons in the visual pathway (Pillow et al., 2008). This approach has been used previously in *Drosophila* larvae to understand sensorimotor integration (Gepner et al., 2015, 2018; Klein et al., 2015; Salazar-Gatzimas et al., 2016) and in zebrafish to investigate the response to fluctuations in heat (Haesemeyer et al., 2015) or to understand the involvement of the hypothalamus in prey capture (Muto et al., 2017).
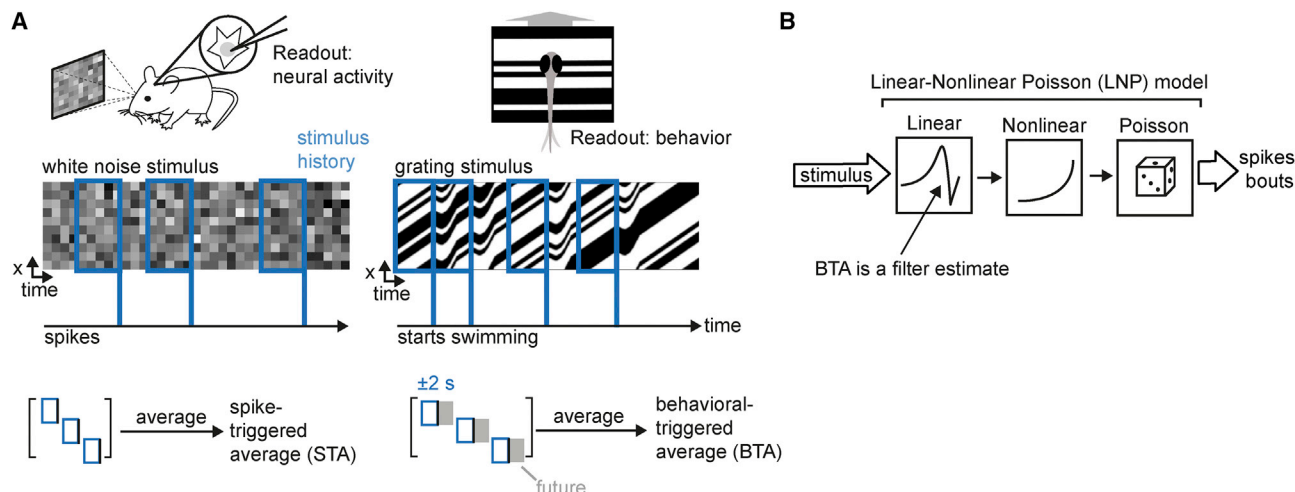
Figure 1. Methodology of Study

(A) We utilize the spike-triggered average commonly used in describing receptive fields of neurons. In our case, we use a binary stimulus that moves forward in time and reacts to fish behavior (moving back briefly during fish swimming). We not only look at the history leading to a bout (blue outline; this yields a linear filter as shown in B) but also at the future to determine whether some structure is persistent during behavior.

(B) The linear filter gained from (A) (the behavioral triggered average [BTA]) can be used in a linear-nonlinear-Poisson (LNP) model to describe the stimulus-behavior relationship.

In a similar way, we present visual stimuli consisting of black and white bars of randomly varying widths moving at different speeds in a caudal to rostral direction and define a behavioral triggered average (BTA) as the average of the visual stimuli that resulted in the head-restrained larva performing an OMR swimming bout (Figure 1A, right panel). We show that the optimal stimulus that evokes the OMR consists of two features: whole-field, global forward motion and a caudal to rostral light to dark luminance transition crossing the larva's head, which has not been previously described in the literature. In addition, we perform whole-brain imaging experiments and identify neural populations, downstream of retinal ganglion cells, that react to the BTA and may play a role in driving the OMR.

RESULTS

The Optomotor Response Is Preferentially Elicited after a Light-Dark Transition

To determine the spatiotemporal luminance features that induce forward-swimming behavior, we presented head-restrained larval zebrafish with a forward-moving whole-field visual stimulus consisting of black and white bars from below (Figure 2A). Explicitly, the visual scene was divided into a number of strips that extended from left to right orthogonally to the axis of the fish, and each strip was randomly chosen to be black or white (see STAR Methods). The strips moved forward, i.e., in a caudal to rostral direction, and as the forward-most disappeared, a new randomly colored strip appears in the caudal visual field, such that the average visual stimulus across the field was gray. Using real-time behavioral tail tracking, we provided the fish visual feedback by changing the visual stimulus speed in proportion to the swimming strength of the fish (Figures 2A and 2B; Video S1; Portugues and Engert, 2011). We chose a closed-loop

setting, because fish show a higher variation in behavior in an open-loop setting (Mu et al., 2019; Portugues and Engert, 2011). For every fish, we computed the reverse correlation of the presented visual stimulus with behavioral onset to obtain the average stimulus that leads to swimming, which we call the behavior-triggered stimulus average or BTA (see STAR Methods and Figures 1A and 2B). The BTA consists of a spatiotemporal filter (the 2 s preceding bout start in Figure 2C) that is stereotypical across individuals (Figure S1A).

The BTA filter is globally largely unstructured 1 to 2 s before bout start. The structure that strongly emerges around 500 ms before bout start comprises a local light and dark luminance band moving forward with respect to the fish. Bout start coincides with the border between the light and dark area reaching the head of the fish (Figures 2C, 2D, and S1B). The fish experiences this light-dark transition (Figures 2E and 2G) with a peak-to-peak duration of around 500 ms. These luminance changes are very local, roughly ±5 mm away from the head of the fish (Figure 2F), which is roughly the length of a larva. The results shown in Figures 2D and 2F further indicate that fish do not start swimming at the local luminance minimum but rather on the light-dark transition itself. Half a second after bout onset, the average luminance levels of the filter are not different from the luminance levels during the unstructured period before bout onset (Figures 2E and 2G). To verify that the BTA can be interpreted as in an STA-based LNP model, we computed the nonlinearity (see STAR Methods and Schwartz et al., 2006) and found an asymmetric point nonlinearity (Figure S1C), which indicates the validity of our approach.

In order to confirm these results, we repeated these experiments with higher spatial and temporal resolution to overcome technical limitations and to better extract the exact stimulus presented in the near visual field of the fish (see STAR Methods). These findings confirmed that the filter indeed shows that fish
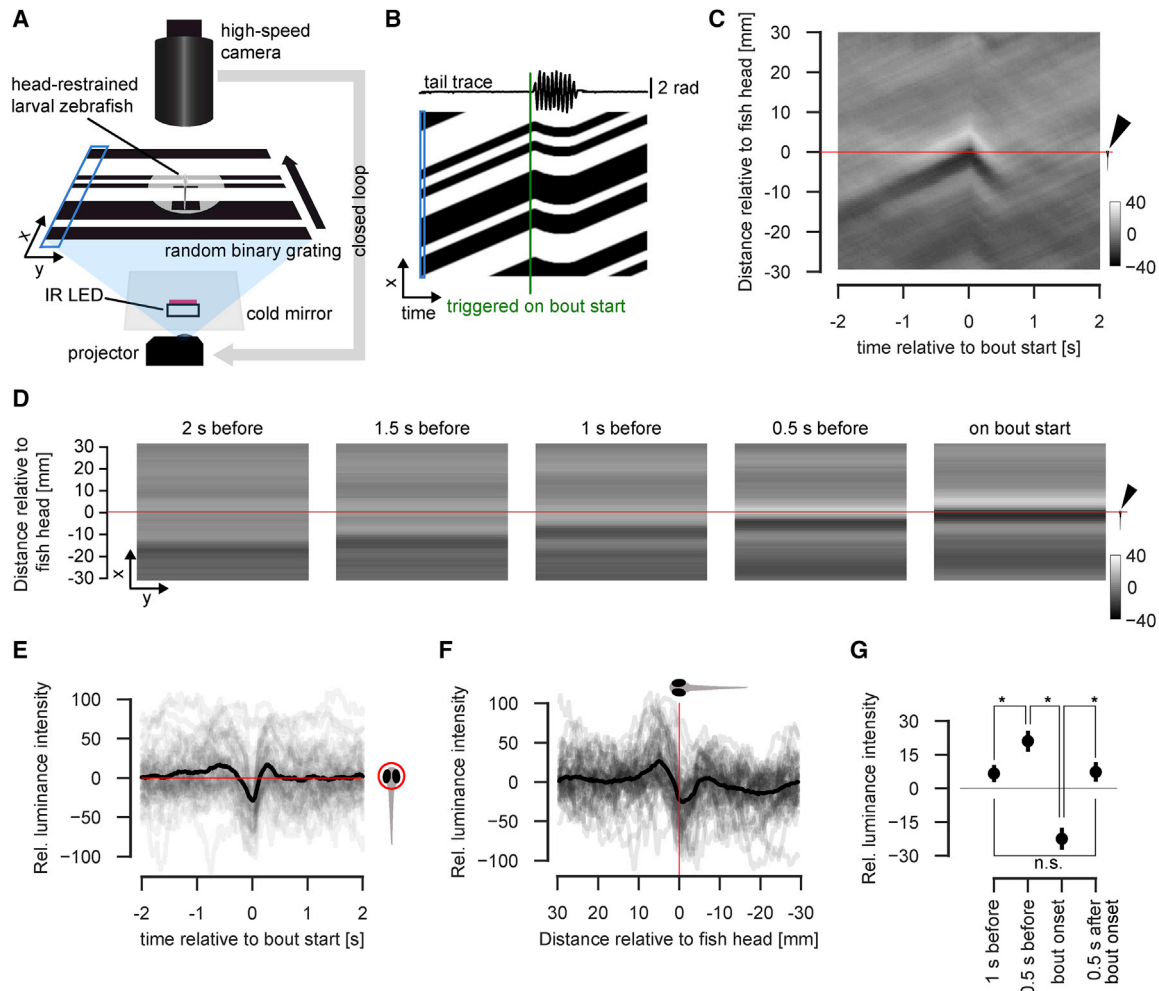
Figure 2. The Optomotor Response Is Preferentially Elicited after a Light-Dark Transition

(A) Schematic of the behavioral setup. A forward-moving binary grating is presented from below to a head-restrained, tail-freed zebrafish larva. The grating is generated in 1D (x, blue rectangle) and stretched in y.

(B) Spacetime diagram showing how the stimulus reacts to the fish swimming in closed loop, where the 2D stimulus is represented in just 1D (blue rectangle as in A). The tail trace is extracted in real time. The BTA is generated by averaging all these spacetime diagrams extending 2 s before and after bout start.

(C) The BTA resulting from averaging the individual BTAs of 52 fish. The position of the fish's head is indicated by the red line, and positive Y values denote positions in front of the fish. The larva on the right, indicated by the black arrowhead, is drawn to scale. The z-scale denotes luminance intensity variations from baseline.

(D) The average visual stimulus in 500-ms steps leading to bout start. As in (C), the fish's position is indicated with a red line and black arrowhead.

(E) The average luminance profile over time on fish head across fish (black) with averages for individual fish (light gray).

(F) Average luminance intensity across fish (black) relative to fish's position with averages for individual fish (light gray).

(G) Average luminance across fish on fish head at 1 s and 500 ms before bout onset, on bout onset, and 500 ms after bout onset. Note that luminance levels 1 s before and 500 ms after the bout onset do not differ. Error bars indicate SEM.

See also Figures S1 and S2.

swim at a local light-dark transition (Figure S1D). Grayscale stimuli, such as square-wave and sinusoid gratings, have been often used in the literature, but the preference to swim exactly at the interface between a light to dark transition has not been previously described. We therefore investigated whether fish prefer a light-dark transition (off edge) in contrast to a dark-light transition (on edge). We found across different luminance settings that swimming does indeed occur preferentially at a light-dark transition (Figure S1E). This effect is dependent on the spatial frequency. Higher spatial frequencies promote bout onsets at

the light-dark transition. With very low spatial frequencies, the stimulus essentially reduces to on and off edges, with almost no whole-field motion. Here, the behavior is well balanced across on and off edges, though there is still a small preference for off edges (Figure S1F).

As we observed structure in the average stimulus that triggers behavior, we next asked whether there was a similar structure in the stimulus ending the bouts: is the immediate goal of a swim bout to obtain a given visual scene? We therefore performed a similar analysis for bout ends. In contrast to bout starts, we found
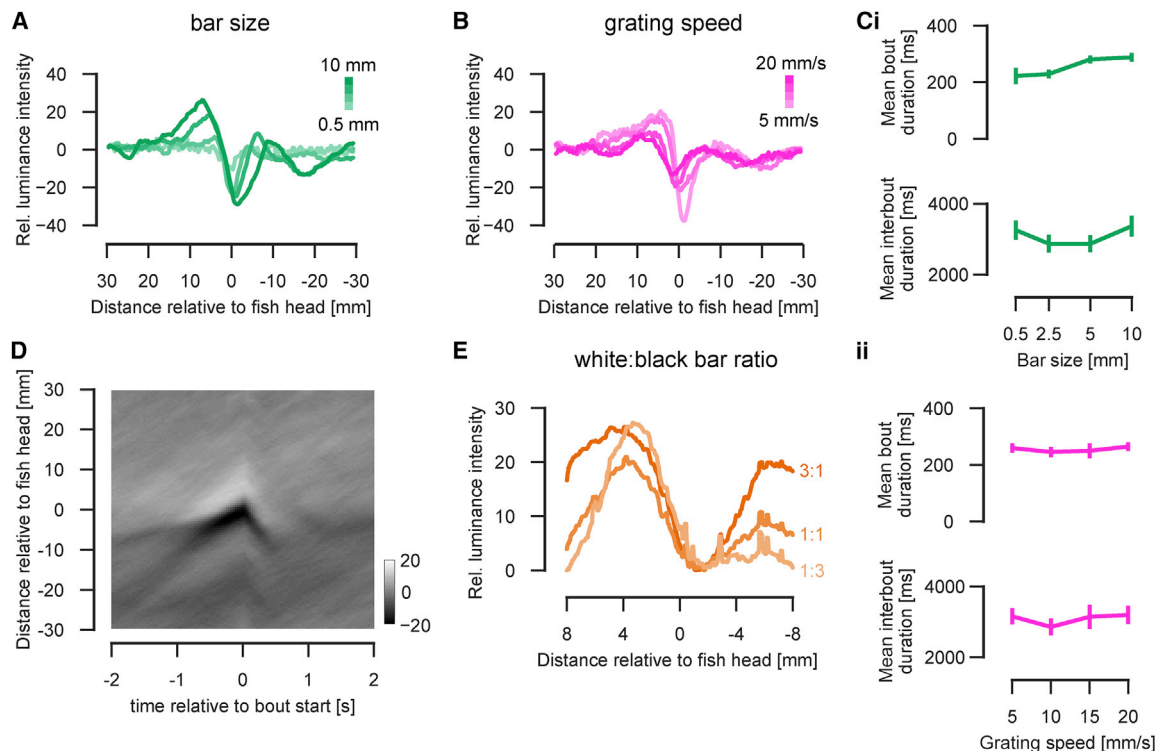
Figure 3. The Behavioral Receptive Field Filter Is Independent of Grating Properties

(A) Mean luminance intensity profiles at bout start for different bar sizes (0.5 mm, 2.5 mm, 5 mm, and 10 mm; shown from light to dark green).

(B) Mean luminance intensity profiles for different grating speeds (5, 10, 15, and 20 mm/s shown in light to dark magenta).

(C) Mean bout and interbout duration for different bar sizes (i) and grating speeds (ii), respectively, for 16 fish. Error bars indicate SEM. ANOVA test to find differences of group means revealed no significance (p ≥ 0.078).

(D) Behavioral triggered average for all grating speeds and bar sizes across 52 fish.

(E) Relative intensity profiles aligned to the minimum for a local random binary grating experiment with varying white-to-black bar ratios for 1:3, 1:1, and 3:1, respectively (N = 13).

See also Figure S3.

no apparent structure in the bout end-triggered average filter (Figure S2A). As suggested by Figures 2E and S2B, we tested whether the emergence of an unstructured gray stimulus once a swimming bout is initiated is able to trigger the ending of the bout. We performed an experiment where the whole visual field turns gray after the detection of bout onset. In this paradigm, fish swim for a significantly shorter time (367 ± 13 versus 328 ± 13 ms; p < 0.05; Student's t test; Figure S2C), but this effect was very small, indicating that the local luminance levels are important to trigger swimming but that other factors may contribute to controlling swim duration and active bout ending.

In summary, these experiments show that a forward-moving, whole-field visual stimulus preferentially elicits swimming when it coincides with a light-dark transition that is local, namely close to the fish's head.

Light-Dark Transition and Behavior Is Largely Unaffected by Stimulus Parameters

To further understand the visual features that optimally drive OMR swimming, we next investigated how the BTA filter depends on the stimulus parameters, as it has been shown pre-

viously that grating speeds influence behavior (Portugues et al., 2015; Severi et al., 2014). Changing the bar width or stimulus speed (defined as the stimulus speed without the closed-loop effect from the fish's behavior) did not affect the most salient features of the filter (compare Figure 2F and Figures 3A and 3B), namely the light to dark transition centered on the larva's head. Small changes in filter features, such as increased peak-to-peak magnitude can be accounted by the different stimulus statistics (Figures 3A and S3A). With slow stimulus speeds, the light-dark transition is pronounced, and this fades with increasing speeds, suggesting that fish behavior involves sensorimotor processing delays and that faster speeds result in increased behavioral jitter (Figures 3B and S3B). Behavioral parameters, such as the mean bout duration and the mean interbout duration (i.e., time between bouts), are not affected by these changes in stimulus parameters (Figure 3C; ANOVA across groups; p ≥ 0.078). The BTA across stimulus parameters (Figure 3D) is very similar to the one shown in Figure 2C, though it reflects the variance of the different stimulus parameters shown in Figures 3A and 3B.

We next addressed the dependence of the BTA on the average global luminance levels. We therefore varied the ratio of white to black bars such that the temporal and spatial average was either lighter or darker gray. A ratio of 3:1 of white:black bars indicates that there are three times more white bars in the whole stimulus than black bars. When determining the BTA filter for these different white:black bar ratio stimuli, we observed a similar light dark transition compared to the BTA shown in Figure 3D, indicating that fish likely adapt to the average luminance level of the stimulus (Figures 3E and S3C). We also verified that the fish behavior and filter nonlinearities remained constant across white:black bar ratios (Figures S3D and S3E).

In certain cases, reverse correlation may not reveal all the stimuli that drive a response. For example, if both a stimulus and its inverse are equally likely to elicit a behavior, then the average of these stimuli would have little structure (Schwartz et al., 2006). We therefore performed behavior-triggered covariance analysis (Schwartz et al., 2006; STAR Methods) on our dataset, focusing on the 2 s prior to bout start to look for evidence of symmetric filters (Figure S4A). Using singular-value decomposition on the covariance matrix, we computed the eigenvectors and eigenvalues of the stimulus covariance matrix. We performed the same analysis on our dataset with shuffled bout start labels, which gives a BTA of homogeneous gray. We sorted the eigenvalues in descending order and found that eigenvalues in both the true and shuffled datasets were very similar to each other, with those from the shuffled dataset tending toward explaining slightly more variance than those from the true dataset (largest eigenvalue 8.1% versus 7.1% of total variance; Figure S4B). When looking at the eigenvectors, we found that the eigenvectors were also very similar across both datasets. The eigenvectors cover a whole-field, global forward-moving sine-like stimulus that increases its frequency with increasing eigenvectors (Figure S4C). Later eigenvectors do not show any structure compared to first eigenvectors (Figure S4C). The covariance analysis returns filters (eigenvectors) with symmetric nonlinearities (in contrast to the BTA), indicating that the filters (shown in Figure S4C) and their inverse contribute equally and result in gray as seen in the BTA periphery. However, given the similarities between the true and the shuffled data (Figure S4C), our interpretation is that these symmetric filters capture general forward whole-field motion and do not contribute acutely to the bout start in the same way that the light-dark transition does in the BTA.

To summarize, we have shown that the BTA's light-dark transition is stable across a variety of stimulus conditions, which highlights the importance of the BTA in eliciting OMR swimming. In addition, together with our covariance analysis, this suggests that symmetric global whole-field motion accompanied by a local light to dark transition close to the larva's head is an integral part of the OMR.

### Luminance and Motion Cues Differentially Shape the Timing and Frequency of the OMR

To precisely examine the importance of both global and local motion in eliciting OMR swimming, we presented larvae with visual stimuli that differentially provide relevant global and local information (Video S2). The first one, which we refer to as filter replay, consisted of the BTA as shown in Figure 3D. It is replayed to the fish as shown in Figure 2D for the full duration of 3 s before and after the optimal visual trigger for the bout. The second, which we term whole-field motion, consisted of the BTA's luminance profile at bout start (see Figures 2F and S5B) stretched in two dimensions and moved over the fish in a caudal to rostral direction. The third stimulus consisted of the BTA shuffled in space (i.e., at every instance in time, the spatial profile of the BTA was shuffled), to avoid motion inducing two-point correlations and maintain the global temporal luminance values. Different visual stimuli properties are shown for comparison in Figure S5.

By construction, the BTA should correspond to the close-to-ideal stimulus that evokes the behavior. Note, however, that the BTA, as opposed to the binary gratings that were used to compute it, contains mostly local and not global motion and is largely unstructured (Figure 2D). We found that the filter replay was indeed capable of evoking swimming (Figures 4A and 4B). However, we were surprised to observe that the whole-field motion stimulus was more effective than the filter replay in eliciting swims. This suggests that whole-field motion is an important feature for triggering OMR swimming, even though its structure seems to be unimportant (see Figure 2C). In addition, swims in response to the whole-field motion stimulus occurred closer to the predicted time of bout start (defined as the time when the stimulus with respect to the fish resembles that last panel in Figure 2D), whereas filter replay-elicited bouts occurred earlier than expected (Figures 4A and 4B). We therefore hypothesized that it was the difference in the stimulus presented in the far visual field that was responsible for the different behavioral profiles observed between the filter replay and the whole-field motion stimulus.

To test this hypothesis, we presented fish with the filter replay locally, in a ±8-mm window surrounding the larva, and combined this with different stimuli in the far caudal visual field (see Figures 4C and S5A and STAR Methods). As a control, we included in this experiment the whole-field motion stimulus as presented in Figures 4A and 4B. The results show that this whole-field motion stimulus again elicited the most swimming (Figure 4D). All other conditions exhibited similar behavioral profiles with fewer bouts elicited and with early timing (Figure 4D). Notably, the stimulus with a local light-dark transition and whole-field motion in the caudal field (Figure 4D, yellow) showed the same early timing as the filter replay. It did elicit, however, more bout starts, suggesting that the timing might be dependent on the light-dark transition and the number of bouts on the whole-field motion (Figure 4D).

We analyzed these local luminance transitions for the stimuli we presented and noticed that the luminance gradient of the whole-field motion stimulus was more pronounced than that of the filter replay. Interestingly, the onset of bouts was mostly concentrated during this light-dark gradient, with a steeper gradient resulting in a shorter time window over which swimming would start (Figure 4E). To probe the role of the gradient on the behavioral profile, we introduced a version of the filter replay, which we call temporally squeezed filter replay (filter replay*), which consists of the filter replay squeezed in time to yield a steeper temporal luminance gradient as similar as possible to the whole-field motion stimulus (Figures S5B–S5E). This stimulus elicited a behavioral profile with similar total number of bouts as the filter replay, but their onset was aligned to the expected bout
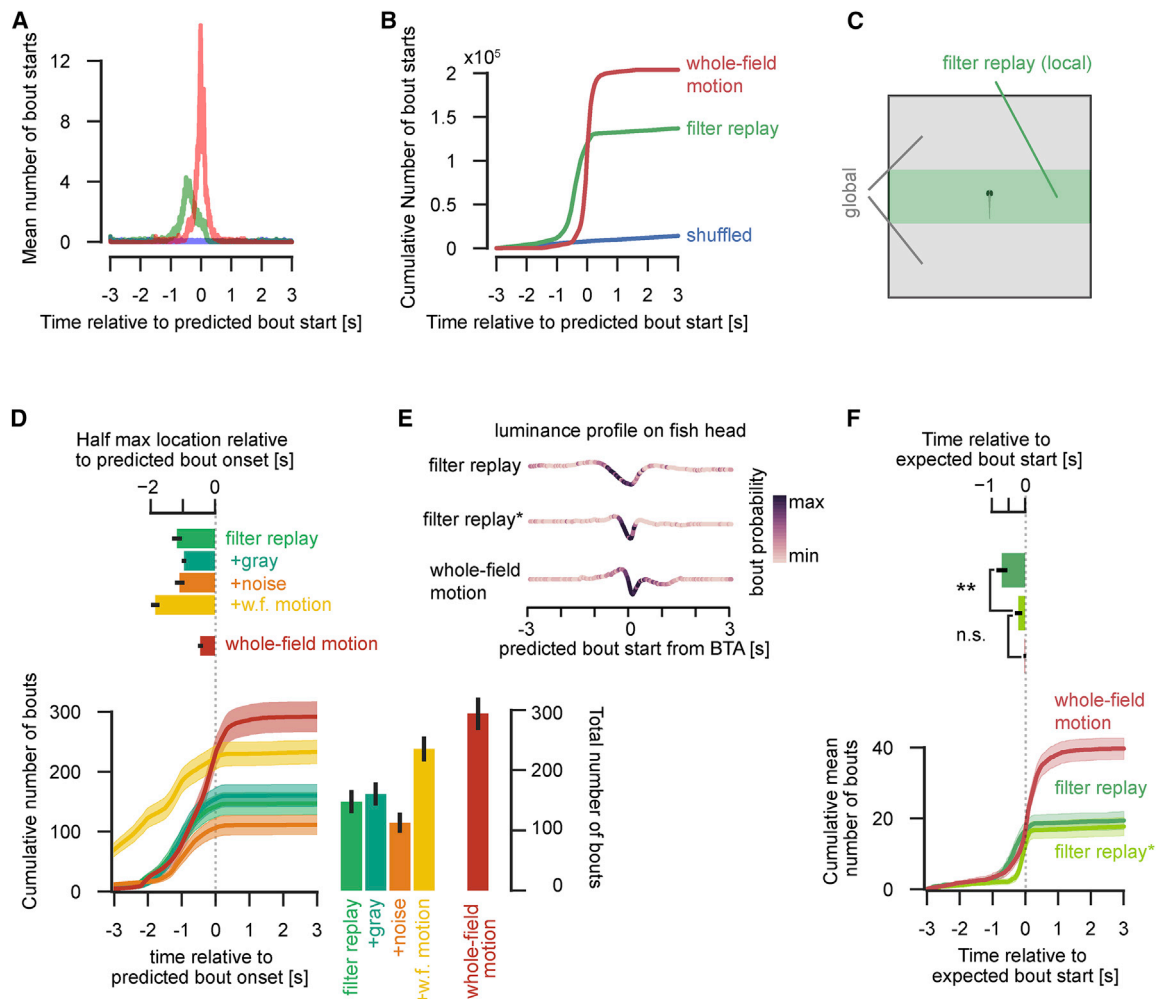
Figure 4. Whole-Field Filter, but Not Filter Replay, Evokes Predicted Behavior

(A) Mean number of bout starts at given time points relative to predicted bout start. Blue lines represent when the grating was shuffled, green filter replay, and red whole-field motion of average trigger (N = 28).

(B) Cumulative distribution of bout starts (shuffled = 1,414; filter replay = 13,699; whole-field motion = 20,380) as shown in (A). The midpoint for filter replay is −4.1 s before predicted bout start; for whole-field motion, it is −0.15 s. The shuffled bouts are distributed equally across the trial. Colors are as in (A).

(C) Schematic of experimental design. Filter replay is shown locally, close to the fish in an ±8-mm window (rostral to caudal; complete stimulus window lateral to the fish), and in the periphery, the stimulus is altered (global).

(D) Cumulative sum of bouts in time depending on stimulus. Either filter replay (green), filter replay with gray in the periphery (turquoise), filter replay with noise (orange), filter replay with whole-field motion (yellow), or the whole-field motion filter (red) as shown in (B) were presented to the fish. Peak number of bouts and half maximum location of cumulative sum are derived from sigmoid fits of the data (see STAR Methods). Shaded area indicates SEM.

(E) Luminance profiles on fish head color-coded with bout start probability. Filter replay with an asterisk was adjusted such that the light-dark gradient matches the gradient of the whole-field motion stimulus.
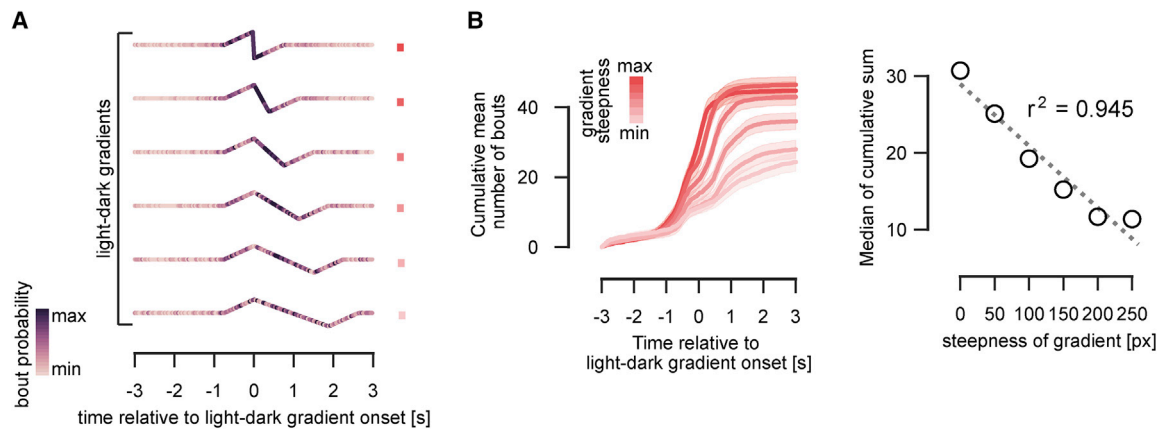
(F) Cumulative sum of mean bout starts across 35 fish. Note that the half maximum as shown above the plot is shifted closer to 0 by squeezing the filter replay gradient in time. Shaded area indicates SEM.

See also Figure S5.

start time just as was the case for the whole-field motion stimulus (Figures 4E and 4F). This confirms the importance of the light-dark luminance gradient in shaping the timing of the behavioral profile and suggests that the missing whole-field motion features lead to reduced number of swimming events as compared to the whole-field motion stimulus.

To confirm the relationship between this luminance gradient and whole-field motion, we presented larvae with visual stimuli that incorporated whole-field motion (similar to the whole field-motion stimulus) and differed only in the local luminance gradient (Figures 5A and S5E). As expected, swim bouts occurred throughout the light-dark transition. Steeper gradients resulted in sharper behavioral profiles, although surprisingly, stimuli with steeper gradients also elicited more bouts despite the fact that whole-field motion was still present (Figure 5B).

Figure 5. Light-Dark Gradient Is Shaping Behavioral Response

(A) Luminance profiles as in Figure 4E for different gradients. The squares indicate the color of the respective trace in (B).

(B) Cumulative sums of mean bout starts across 35 fish, color-coded depending on gradient slope (light colors shallow; dark colors steep gradient; see squares in A). Shaded area indicates SEM. Right panel shows the half maximum of cumulative sums against steepness of gradient (higher numbers produce shallower gradient).

See also Figure S5.

We investigated to what spatial extent these visual features contribute to behavior. Figure S5F shows that the local environment is important: when providing neither motion nor light-dark transitions, the behavioral response was significantly reduced compared to whole-field sine gratings. When providing motion and light-dark transitions only in the local vicinity, behavior was robustly evoked. It is important to note that the light-dark transition has to be directed and carry motion: if this local edge is substituted for a local homogeneous luminance decrease, behavior was significantly reduced (Figure S5G). Likewise, whole-field luminance changes do not evoke a stereotyped behavior compared to forward, i.e., caudal-to-rostral, moving sine gratings (Figure S5H).

Overall, the results presented in Figures 4 and 5 show that both the local luminance gradient and the presence of whole-field motion contribute to shaping the behavioral profile. In certain circumstances, whole-field motion is required to elicit a stronger behavioral response (Figures 4A, 4B, 4D, and 4F). The light-dark luminance gradient shapes the behavioral response distribution and its peak onset (Figures 4B, 4F, and 5B). However, this gradient may also affect the number of bouts elicited (Figure 5B), suggesting a nuanced interplay between the local and global motion percept.

Neural Responses Are Tuned to Behaviorally Relevant BTA Whole-Field Motion

Having defined a visual filter that drives the OMR, we were interested in investigating whether there were any neuronal responses specific to this filter. We therefore performed two-photon, whole-brain functional imaging in larvae pan-neuronally expressing the genetically encoded calcium indicator GCaMP6s (Kim et al., 2017). We presented the fish with five stimuli that incorporated whole-field motion and light-dark luminance transitions in diverse ways: a sharp light-dark transition (commonly known as off edge) moving forward across the visual scene; a smooth dark-to-light whole-field luminance transition; a

forward-moving sine grating; and finally the whole-field filter, first moving forward and then the reversed filter moving backward (Figure 6A). This later stimulus was presented because it has the opposite sign of motion, but it exhibits the same light-to-dark transition. Only the sine grating and the forward-moving whole-field filter are able to elicit reliable behavior (Figure 6B). This is in line with our previous findings that low spatial frequencies and whole-field luminance changes evoke only little to no behavior (Figures S1F and S5H).

Using pixel-wise correlations (Portugues et al., 2014), we found 440,736 active regions of interests (ROIs) from nine fish that include cell somata and neuropil (see Figure S6A for coverage). We grouped ROIs into clusters with distinct responses using unsupervised clustering (Figures S6B and S6C; see also STAR Methods) and found five that were reliably and selectively responsive to the filter or its reverse (Figure 6B). 3D representations of the found clusters are shown in Video S3. Clusters 1 and 5 showed luminance-dependent responses corresponding to luminance on and off, respectively. Cluster 1 includes the medial cerebellum, as well as several retinal ganglion cell arborization fields (AFs), in particular AF9. Cluster 5 includes active units in the pretectum, dorsal thalamus, and bilateral strata of the tectal neuropil. Cluster 3 responded specifically to the reversed filter that moves backward and thus comprises a reverse motion cluster. ROIs in cluster 3 are mainly located in rhombomere 1 of the hindbrain and the tectal stratum periventriculare. Cluster 4 was active for all visual motion, regardless of the direction (Figures 6B and 6C). It includes the tectal neuropil, as well as other arborization fields and some cells ventral to the tectum. Only cluster 2 had responses more specific to the forward-moving filter. This cluster was also active when presented with the forward-moving off edge, a feature shared with the forward filter, but not when the reversed filter is shown, which has the same luminance transition but with the opposite sign of motion (Figure 6B). These responses are spread out over the whole brain (Figure 6C). They include the nucleus of the medial
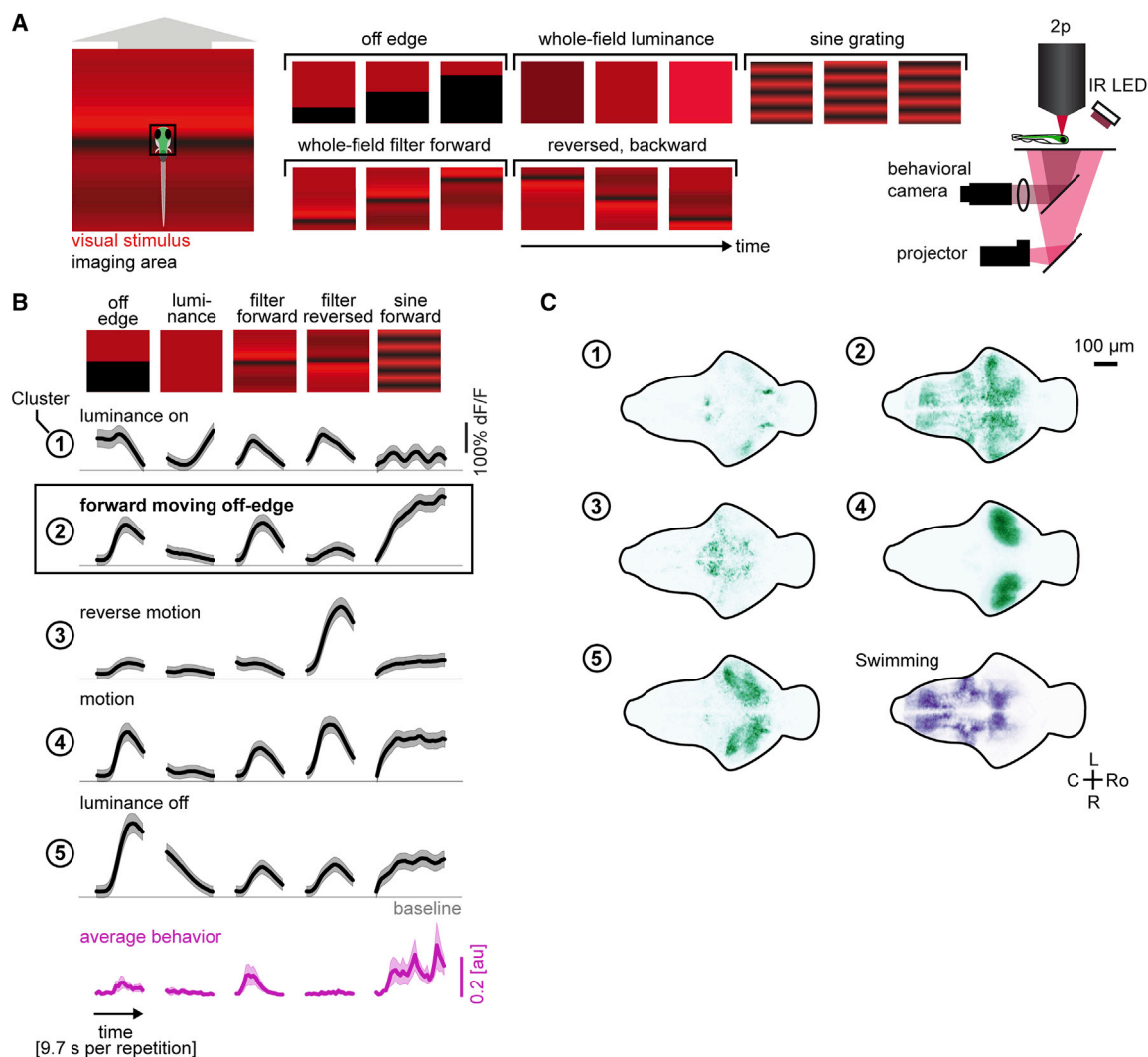
Figure 6. Two-Photon Calcium Imaging Shows Neural Assemblies Preferentially Tuned to Filter Components

(A) Visual stimuli comprising different filter features were shown to larvae expressing pan-neuronally GCaMP6s in a two-photon setup.

(B) Black lines represent the mean fluorescence traces of ROIs in a given cluster compared to their baseline fluorescence (gray). Responses are shown as means across stimulus repetitions; the shaded area indicates the SEM. The average behavior (measured by swimming vigor; see STAR Methods) for each stimulus is shown in magenta below the fluorescent traces. Shaded area indicates the SEM.

(C) Z-projection maps of ROIs found in N = 9 fish corresponding to a given cluster (green) or ROIs that are highly correlated (r > 0.8) with swimming vigor (purple). See also Figure S6.

longitudinal fasciculus (nMLF), the pretectum, the tectal neuropil (AF10), and AF6.

When looking at units that are active during swimming episodes, we identified a single cluster related to swimming (Figure 6C). Notably, the cluster specific to the forward filter (cluster 2) contained a very small overlap with this swimming cluster, mainly surrounding the nMLF neurons, indicating that the neurons in cluster 2 are either sensory or directly involved in the sensorimotor transformation that leads to behavior. Further, neurons in cluster 2 had only little correlation with swimming.

In summary, we show tuned responses to the forward-moving filter that are located across the whole fish brain.

A Generalized Linear Model Can Capture More Variance Than Chance

Our results demonstrate that OMR swimming is triggered both by a light-dark transition and whole-field motion. We asked whether a generalized linear model, a variant of the LNP model (Figure 1B), can predict the fish's behavior as previously shown for heat-induced swimming in larval zebrafish (Haesemeyer et al., 2015, 2018). At every instance in time, we fed the grating history computed over a 1 s window together with the bout starts as labels to the generalized linear model (GLM) fitting algorithm that finds the ideal filter using log-likelihood (Figure S7A). In agreement with our analysis, the GLM filter looks very similar to the BTA (Figure S7A). The GLM returns rates that should
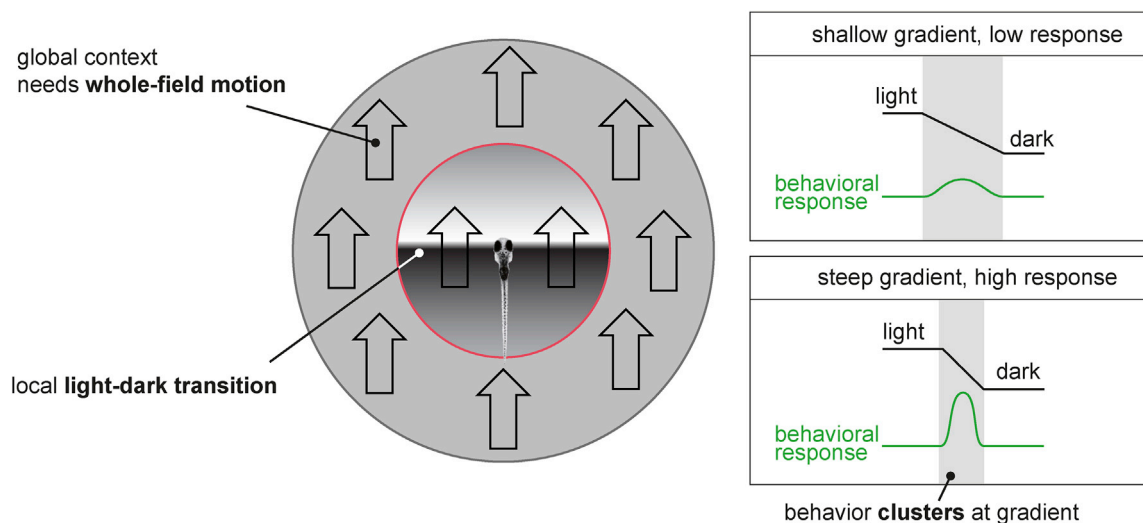
Figure 7. Optomotor Swimming Is Strongly Induced by Local Light-Dark Transition and Peripheral Whole-Field Motion
Our working model suggests that OMR is induced by peripheral whole-field motion, with no specific structure (outer, gray circle with motion-indicating arrows) and local light-dark transitions (inner circle). The behavior is clustered at the local light-dark gradient, and the gradient's steepness modulates the behavioral response: the steeper the gradient, the higher the behavioral response (see two example boxes).

coincide with bouts (Figure S7B). We assessed model specificity and sensitivity, as well as false-positive and false-negative rates (Figure S7C). For every given threshold and model (Figure S7B), we computed the percentage of peaks that are accompanied by a bout (i.e., true predictive value; Figure S7D) and the percentage of bouts that are accompanied by a peak (i.e., true positive rate; Figure S7E). The GLM is capable of explaining a higher amount of variance compared to bootstrap controls. Up to 13.2% of the detected peaks above threshold are accompanied by a bout, whereas 48.0% of the bouts are accompanied by a peak (compared to 8.6% and 21.0% in bootstrap controls, respectively; Figures S7D and S7E). When determining the false-negative and false-positive rates for our model, we observe that the model outperforms the bootstrap control (Figure S7F). Overall, the simple GLM succeeds in explaining the data better than chance, though we expect more complex models to be able to improve this significantly.

DISCUSSION

In this study, we used a reverse-correlation approach to identify the stimulus that is optimal in eliciting the forward optomotor response. We found that this stimulus consists of two features: spatially symmetric global whole-field motion and an asymmetric, forward-moving, light-dark transition occurring locally at the larva's head. The luminance gradient of this transition influences the swimming rate and timing of the bouts, with steeper gradients eliciting more bouts whose onsets are temporally closer aligned with the stimulus. Although a contribution of whole-field motion was expected from previous OMR studies, the importance of a local light-dark transition has not been described before.

Different features of whole-field motion that lead to behavioral modulation have been probed before in the context of the OMR,

such as contrast, temporal, and spatial frequency in flies (Buchner, 1976; Creamer et al., 2018; Fry et al., 2009; Haag et al., 2004; Katsov and Clandinin, 2008; Silies et al., 2013; Theobald et al., 2008) and speed in zebrafish larvae (Portugues et al., 2015; Severi et al., 2014). Asymmetries in the processing of light and dark stimuli have been shown to exist in zebrafish but always relating to behaviors that involve local or object-related motion, such as prey capture, looming stimuli, or visually evoked responses (Bianco and Engert, 2015; Burgess and Granato, 2007; Burgess et al., 2010; Dunn et al., 2016; Emran et al., 2007; Semmelhack et al., 2014; Temizer et al., 2015). These studies show that luminance on and off responses are processed very differently in the zebrafish brain, consistent with our results shown in Figure 6, where the clusters 1 and 5 show very little overlap. In the context of the OMR, experiments in flies, dragonflies, and primates (Clark et al., 2014; Leonhardt et al., 2016; Nitzany et al., 2017) have shown asymmetries in the processing of light and dark in the on and off pathways using two- and three-point correlation glider stimuli (Hu and Victor, 2010). Furthermore, the differential contribution of the on-off symmetric whole-field motion in the periphery and the local off edge is reminiscent of the figure-ground distinctions that have been probed in flies (Aptekar et al., 2015; Barnhart et al., 2018; Fox et al., 2014), although the systematic analysis of local and global motion percepts or object motion superimposed on a moving background has not been investigated in larval zebrafish.

In zebrafish, axons from RGCs are known to project to ten AFs (Burrill and Easter, 1994; Robles et al., 2014). It is likely that the two features that we describe in this study, namely on/off-independent whole-field motion and the local forward-moving off edge, are conveyed by different RGCs, possibly to different AFs.

Our simple generalized linear model showed moderate success in explaining the observed behavior. As our visual stimulus carries high temporal correlation, the calculated filter may be

biased to the real underlying filter and thus lowers the estimation quality of our model. The filter can also be stochastically biased by the fact that swimming follows very likely a Poisson process (Portugues et al., 2015). Further behavioral experiments accompanied by modeling studies need to be performed to understand the interaction between the two visual features that contribute to the OMR. If indeed different RGCs convey these features to different AFs, these models could provide a means to create hypotheses about the convergence of different visual streams and the neuronal mechanisms that could mediate this interaction, such as neuromodulation, gating, or gain control.

Our preliminary imaging study was able to identify units tuned specifically to visual stimuli known to drive the OMR. Interestingly, we observe that units that respond to behavior-inducing stimuli occur throughout the brain but are enriched in the pretectum and AF6, areas that were recently suggested to contribute to OMR and behavior (Kramer et al., 2019; Kubo et al., 2014; Naumann et al., 2016). Here, we provide further evidence that these areas are indeed important for the OMR, as they also respond to the light-dark transition feature we describe.

To summarize, we propose a working model (Figure 7) in which the OMR is strongly induced by a whole-field motion percept that is light-dark symmetric, together with a newly described, forward-moving local light-dark transition. The behavioral response to the OMR is further modulated by the steepness of the light-dark gradient, which may explain the known dependence of this behavior on visual features, such as contrast and temporal and spatial frequency. This study shows that the OMR, a paradigm that has been extensively used, is still not fully understood, and its comprehensive characterization will undoubtedly reveal further insights into the neuronal circuitry underlying behavior.

STAR★METHODS

Detailed methods are provided in the online version of this paper and include the following:

- KEY RESOURCES TABLE
- LEAD CONTACT AND MATERIALS AVAILABILITY
- EXPERIMENTAL MODEL AND SUBJECT DETAILS
- METHOD DETAILS
  - Behavioral Setup
  - Stimulus Generation and Presentation
  - Behavioral Triggered Average
  - Behavioral Triggered Covariance Analysis
  - Binary Grating Edge Detection
  - Luminance Experiments
  - Filter Replay
  - Functional Imaging
  - Image Analysis
  - Generalized Linear Model
- QUANTIFICATION AND STATISTICAL ANALYSIS
- DATA AND CODE AVAILABILITY

SUPPLEMENTAL INFORMATION

Supplemental Information can be found online at https://doi.org/10.1016/j.celrep.2019.09.024.

REFERENCES

Ahrens, M.B., Li, J.M., Orger, M.B., Robson, D.N., Schier, A.F., Engert, F., and Portugues, R. (2012). Brain-wide neuronal dynamics during motor adaptation in zebrafish. Nature 485, 471–477.

Aptekar, J.W., Keleş, M.F., Lu, P.M., Zolotova, N.M., and Frye, M.A. (2015). Neurons forming optic glomeruli compute figure-ground discriminations in Drosophila. J. Neurosci. 35, 7587–7599.

Barnhart, E.L., Wang, I.E., Wei, H., Desplan, C., and Clandinin, T.R. (2018). Sequential nonlinear filtering of local motion cues by global motion circuits. Neuron 100, 229–243.e3.

Bianco, I.H.H., and Engert, F. (2015). Visuomotor transformations underlying hunting behavior in zebrafish. Curr. Biol. 25, 831–846.

Borst, A., Haag, J., and Reiff, D.F. (2010). Fly motion vision. Annu. Rev. Neurosci. 33, 49–70.

Buchner, E. (1976). Elementary movement detectors in an insect visual system. Biol. Cybern. 24, 85–101.

Burgess, H.A., and Granato, M. (2007). Sensorimotor gating in larval zebrafish. J. Neurosci. 27, 4984–4994.

Burgess, H.A., Schoch, H., and Granato, M. (2010). Distinct retinal pathways drive spatial orientation behaviors in zebrafish navigation. Curr. Biol. 20, 381–386.

Burrill, J.D., and Easter, S.S., Jr. (1994). Development of the retinofugal projections in the embryonic and larval zebrafish (Brachydanio rerio). J. Comp. Neurol. 346, 583–600.

Chen, X., Mu, Y., Hu, Y., Kuan, A.T., Nikitchenko, M., Randlett, O., Chen, A.B., Gavornik, J.P., Sompolinsky, H., Engert, F., and Ahrens, M.B. (2018). Brainwide organization of neuronal activity and convergent sensorimotor transformations in larval zebrafish. Neuron 100, 876–890.e5.

Clark, D.T. (1981). Visual responses in developing zebrafish (Brachydanio rerio). PhD dissertation (University of Oregon).

Clark, D.A., Fitzgerald, J.E., Ales, J.M., Gohl, D.M., Silies, M.A., Norcia, A.M., and Clandinin, T.R. (2014). Flies and humans share a motion estimation strategy that exploits natural scene statistics. Nat. Neurosci. 17, 296–303.

Creamer, M.S., Mano, O., and Clark, D.A. (2018). Visual control of walking speed in Drosophila. Neuron 100, 1460–1473.e6.

DeCharms, R.C., and Merzenich, M. (1998). Characterizing neurons in the primary auditory cortex of the awake primate using reverse correlation. In Advances in Neural Information Processing Systems 10, M.I. Jordan, M.J. Kearns, and S.A. Solla, eds. (NIPS), pp. 124–130.

Dieringer, N., Precht, W., and Blight, A.R. (1982). Resetting fast phases of head and eye and their linkage in the frog. Exp. Brain Res. *47*, 407–416.

Dunn, T.W., Gebhardt, C., Naumann, E.A., Riegler, C., Ahrens, M.B., Engert, F., and Del Bene, F. (2016). Neural circuits underlying visually evoked escapes in larval zebrafish. Neuron *89*, 613–628.

Emran, F., Rihel, J., Adolph, A.R., Wong, K.Y., Kraves, S., and Dowling, J.E. (2007). OFF ganglion cells cannot drive the optokinetic reflex in zebrafish. Proc. Natl. Acad. Sci. USA *104*, 19126–19131.

Fox, J.L., Aptekar, J.W., Zolotova, N.M., Shoemaker, P.A., and Frye, M.A. (2014). Figure-ground discrimination behavior in Drosophila. I. Spatial organization of wing-steering responses. J. Exp. Biol. *217*, 558–569.

Fry, S.N., Rohrseitz, N., Straw, A.D., and Dickinson, M.H. (2009). Visual control of flight speed in Drosophila melanogaster. J. Exp. Biol. *212*, 1120–1130.

Gepner, R., Mihovilovic Skanata, M., Bernat, N.M., Kaplow, M., and Gershow, M. (2015). Computations underlying Drosophila photo-taxis, odor-taxis, and multi-sensory integration. eLife *4*, e06229.

Gepner, R., Wolk, J., Wadekar, D.S., Dvali, S., and Gershow, M. (2018). Variance adaptation in navigational decision making. eLife *7*, e37945.

Haag, J., Denk, W., and Borst, A. (2004). Fly motion vision is based on Reichardt detectors regardless of the signal-to-noise ratio. Proc. Natl. Acad. Sci. USA *101*, 16333–16338.

Haesemeyer, M., Robson, D.N., Li, J.M., Schier, A.F., and Engert, F. (2015). The structure and timescales of heat perception in larval zebrafish. Cell Syst. *1*, 338–348.

Haesemeyer, M., Robson, D.N., Li, J.M., Schier, A.F., and Engert, F. (2018). A brain-wide circuit model of heat-evoked swimming behavior in larval zebrafish. Neuron *98*, 817–831.e6.

Hu, Q., and Victor, J.D. (2010). A set of high-order spatiotemporal stimuli that elicit motion and reverse-phi percepts. J. Vis. *10*, 9.1–9.16.

Katsov, A.Y., and Clandinin, T.R. (2008). Motion processing streams in Drosophila are behaviorally specialized. Neuron *59*, 322–335.

Kim, D.H., Kim, J., Marques, J.C., Grama, A., Hildebrand, D.G.C., Gu, W., Li, J.M., and Robson, D.N. (2017). Pan-neuronal calcium imaging with cellular resolution in freely swimming zebrafish. Nat. Methods *14*, 1107–1114.

Klein, M., Afonso, B., Vonner, A.J., Hernandez-Nunez, L., Berck, M., Tabone, C.J., Kane, E.A., Pieribone, V.A., Nitabach, M.N., Cardona, A., et al. (2015). Sensory determinants of behavioral dynamics in Drosophila thermotaxis. Proc. Natl. Acad. Sci. USA *112*, E220–E229.

Knogler, L.D., Markov, D.A., Dragomir, E.I., Štih, V., and Portugues, R. (2017). Sensorimotor representations in cerebellar granule cells in larval zebrafish are dense, spatially organized, and non-temporally patterned. Curr. Biol. *27*, 1288–1302.

Kramer, A., Wu, Y., Baier, H., and Kubo, F. (2019). Neuronal architecture of a visual center that processes optic flow. Neuron *103*, 118–132.e7.

Kubo, F., Hablitzel, B., Dal Maschio, M., Driever, W., Baier, H., and Arrenberg, A.B. (2014). Functional architecture of an optic flow-responsive area that drives horizontal eye movements in zebrafish. Neuron *81*, 1344–1359.

Leonhardt, A., Ammer, G., Meier, M., Serbe, E., Bahl, A., and Borst, A. (2016). Asymmetry of Drosophila ON and OFF motion detectors enhances real-world velocity estimation. Nat. Neurosci. *19*, 706–715.

Lister, J.A., Robertson, C.P., Lepage, T., Johnson, S.L., and Raible, D.W. (1999). nacre encodes a zebrafish microphthalmia-related protein that regulates neural-crest-derived pigment cell fate. Development *126*, 3757–3767.

Marmarelis, P.Z., and Marmarelis, V.Z. (1978). Analysis of Physiological Systems: The White-Noise Approach (Springer-Verlag).

Matsuo, M., Ando, Y., Kamei, Y., and Fukamachi, S. (2018). A semi-automatic and quantitative method to evaluate behavioral photosensitivity in animals based on the optomotor response (OMR). Biol. Open *7*, bio033175.

Mu, Y., Bennett, D.V., Rubinov, M., Narayan, S., Yang, C.T., Tanimoto, M., Mensh, B.D., Looger, L.L., and Ahrens, M.B. (2019). Glia accumulate evidence that actions are futile and suppress unsuccessful behavior. Cell *178*, 27–43.e19.

Muto, A., Orger, M.B., Wehman, A.M., Smear, M.C., Kay, J.N., Page-McCaw, P.S., Gahtan, E., Xiao, T., Nevin, L.M., Gosse, N.J., et al. (2005). Forward genetic analysis of visual behavior in zebrafish. PLoS Genet. *1*, e66.

Muto, A., Lal, P., Ailani, D., Abe, G., Itoh, M., and Kawakami, K. (2017). Activation of the hypothalamic feeding centre upon visual prey detection. Nat. Commun. *8*, 15029.

Naumann, E.A., Fitzgerald, J.E., Dunn, T.W., Rihel, J., Sompolinsky, H., and Engert, F. (2016). From whole-brain data to functional circuit models: the zebrafish optomotor response. Cell *167*, 947–960.e20.

Neuhauss, S.C., Biehlmaier, O., Seeliger, M.W., Das, T., Kohler, K., Harris, W.A., and Baier, H. (1999). Genetic disorders of vision revealed by a behavioral screen of 400 essential loci in zebrafish. J. Neurosci. *19*, 8603–8615.

Nikolaou, N., Lowe, A.S., Walker, A.S., Abbas, F., Hunter, P.R., Thompson, I.D., and Meyer, M.P. (2012). Parametric functional maps of visual inputs to the tectum. Neuron *76*, 317–324.

Nitzany, E.I., Menda, G., Shamble, P.S., Golden, J.R., Hu, Q., Hoy, R.R., and Victor, J.D. (2017). Neural computations combine low- and high-order motion cues similarly, in dragonfly and monkey. bioRxiv. https://doi.org/10.1101/240101.

Orger, M.B., and Baier, H. (2005). Channeling of red and green cone inputs to the zebrafish optomotor response. Vis. Neurosci. *22*, 275–281.

Orger, M.B., Smear, M.C., Anstis, S.M., and Baier, H. (2000). Perception of Fourier and non-Fourier motion by larval zebrafish. Nat. Neurosci. *3*, 1128–1133.

Orger, M.B., Kampff, A.R., Severi, K.E., Bollmann, J.H., and Engert, F. (2008). Control of visually guided behavior by distinct populations of spinal projection neurons. Nat. Neurosci. *11*, 327–333.

Pillow, J.W., Shlens, J., Paninski, L., Sher, A., Litke, A.M., Chichilnisky, E.J., and Simoncelli, E.P. (2008). Spatio-temporal correlations and visual signalling in a complete neuronal population. Nature *454*, 995–999.

Portugues, R., and Engert, F. (2011). Adaptive locomotor behavior in larval zebrafish. Front. Syst. Neurosci. *5*, 72.

Portugues, R., Feierstein, C.E., Engert, F., and Orger, M.B. (2014). Whole-brain activity maps reveal stereotyped, distributed networks for visuomotor behavior. Neuron *81*, 1328–1343.

Portugues, R., Haesemeyer, M., Blum, M.L., and Engert, F. (2015). Whole-field visual motion drives swimming in larval zebrafish via a stochastic process. J. Exp. Biol. *218*, 1433–1443.

Randlett, O., Wee, C.L., Naumann, E.A., Nnaemeka, O., Schoppik, D., Fitzgerald, J.E., Portugues, R., Lacoste, A.M.B., Riegler, C., Engert, F., and Schier, A.F. (2015). Whole-brain activity mapping onto a zebrafish brain atlas. Nat. Methods *12*, 1039–1046.

Ringach, D.L., Sapiro, G., and Shapley, R. (1997). A subspace reverse-correlation technique for the study of visual neurons. Vision Res. *37*, 2455–2464.

Robles, E., Laurell, E., and Baier, H. (2014). The retinal projectome reveals brain-area-specific visual representations generated by ganglion cell diversity. Curr. Biol. *24*, 2085–2096.

Roeser, T., and Baier, H. (2003). Visuomotor behaviors in larval zebrafish after GFP-guided laser ablation of the optic tectum. J. Neurosci. *23*, 3726–3734.

Rohlfing, T., and Maurer, C.R., Jr. (2003). Nonrigid image registration in shared-memory multiprocessor environments with application to brains, breasts, and bees. IEEE Trans. Inf. Technol. Biomed. *7*, 16–25.

Salazar-Gatzimas, E., Chen, J., Creamer, M.S.S., Mano, O., Mandel, H.B.B., Matulis, C.A.A., Pottackal, J., and Clark, D.A.A. (2016). Direct measurement of correlation responses in Drosophila elementary motion detectors reveals fast timescale tuning. Neuron *92*, 227–239.

Schwartz, O., Pillow, J.W., Rust, N.C., and Simoncelli, E.P. (2006). Spike-triggered neural characterization. J. Vis. *6*, 484–507.

Semmelhack, J.L., Donovan, J.C., Thiele, T.R., Kuehn, E., Laurell, E., and Baier, H. (2014). A dedicated visual pathway for prey detection in larval zebrafish. eLife *3*, e04878.

Severi, K.E., Portugues, R., Marques, J.C., O'Malley, D.M., Orger, M.B., and Engert, F. (2014). Neural control and modulation of swimming speed in the larval zebrafish. Neuron 83, 692–707.

Shi, C., Yuan, X., Chang, K., Cho, K.S., Xie, X.S., Chen, D.F., and Luo, G. (2018). Optimization of optomotor response-based visual function assessment in mice. Sci. Rep. 8, 9708.

Silies, M., Gohl, D.M., Fisher, Y.E., Freifeld, L., Clark, D.A., and Clandinin, T.R. (2013). Modular use of peripheral input channels tunes motion-detecting circuitry. Neuron 79, 111–127.

Štih, V., Petrucco, L., Kist, A.M., and Portugues, R. (2019). Stytra: an open-source, integrated system for stimulation, tracking and closed-loop behavioral experiments. PLoS Comput. Biol. 15, e1006699.

Temizer, I., Donovan, J.C., Baier, H., and Semmelhack, J.L. (2015). A visual pathway for looming-evoked escape in larval zebrafish. Curr. Biol. 25, 1823–1834.

Theobald, J.C., Duistermars, B.J., Ringach, D.L., and Frye, M.A. (2008). Flies see second-order motion. Curr. Biol. 18, R464–R465.

STAR★METHODS

KEY RESOURCES TABLE

REAGENT or RESOURCE	SOURCE	IDENTIFIER
Experimental Models: Organisms/Strains		
Zebrafish Wildtype Tüpfel-Longfin (TL)	N/A	ZFIN: ZDB-GENO-990623-2
Zebrafish Tg(*elavl3*:GCaMP6s)	Kim et al., 2017	N/A
Software and Algorithms		
ImageJ/Fiji	NIH	https://fiji.sc
CMTK	Rohlfing and Maurer, 2003	https://www.nitrc.org/projects/cmtk/
Python 3.6	Anaconda, Inc.	https://www.anaconda.com/distribution
LabVIEW	National Instruments	http://www.ni.com/en-us/shop/labview.html
Stytra	Štih et al., 2019	http://portugueslab.com/stytra/
Other		
Z-brain Atlas	Randlett et al., 2015	https://engertlab.fas.harvard.edu/Z-Brain/

LEAD CONTACT AND MATERIALS AVAILABILITY

Further information and requests for resources and reagents should be directed to and will be fulfilled by the Lead Contact, Ruben Portugues (rportugues@neuro.mpg.de). This study did not generate new unique reagents.

EXPERIMENTAL MODEL AND SUBJECT DETAILS

Adult zebrafish (*Danio Rerio*) were bred in house at the Max Planck Institute of Neurobiology fish facility and kept at a 14/10 h day/night cycle. 6-8 days post fertilization larvae were used for either behavioral or imaging experiments of as yet undetermined sex. For behavioral experiments, we used Tüpfel long-fin (TL) larvae. For imaging experiments, we used a transgenic line that expresses GCaMP6s under the pan-neuronal HuC (*elavl3*) promoter (Kim et al., 2017). These fish were also homozygous for the Nacre mutation (mitfa$^{-/-}$) that interferes with melanophore pigment formation (Lister et al., 1999). All experiments were approved by the Regierung von Oberbayern via TVA 55-2-1-54-2532-82-2016.

METHOD DETAILS

Behavioral Setup
Behavioral experiments were performed using custom-built behavioral setups as described previously (Portugues and Engert, 2011). Stimuli were presented from below using an ASUS P1E or Asus P2E micro projector. The fish's tail was tracked using a high-speed camera (XIMEA MQ003MG-CM or XIMEA MQ022RG-CM), a Navitar tele-objective (TC.5028), an infrared illumination source (Osram 850 nm high power LED) and a 830 nm long-pass filter (Edmund Optics). To directly extract grating position from the camera image, we removed the 830 nm long-pass filter and adjusted the IR LED intensity and exposure time of the camera to ensure both good grating extraction and proper tail tracking. Larvae were embedded in 1.5% low melting point agarose (Thermo Scientific) in a 35 mm Petri dish (Corning) and is roughly 5 mm away from the presented visual stimulus (Severi et al., 2014). The tail was freed to allow the fish to move its tail voluntarily while keeping the head and tail base restrained. Stimuli presentation and online tail tracking was performed using custom-written software in Python using the Anaconda distribution package. Libraries utilized, but not included in Anaconda, were a custom built OpenCV library with enabled XIMEA camera support and pyqtgraph for fast online plotting. Stytra (Štih et al., 2019) was employed for a subset of behavioral experiments.

Stimulus Generation and Presentation
The visual stimulus consists of sequences of binary (i.e., black and white or black and red for functional imaging) bars of given sizes (0.5 mm, 2.5 mm, 5 mm and 10 mm). The stimuli were generated by choosing white and black bars from a uniform distribution to ensure the same average gray value across the whole field. For experiments that probed the filter dependence on white-to-black bar ratio, we changed the proportion accordingly to have on average 25, 50 or 75% white bars. The stimulus presentation was updated at 60 Hz (projector refresh rate). Behavioral experiments were performed in closed-loop, meaning that the fish's behavior was

fed back to the visual stimulus to provide the fish with visual feedback (similar to Portugues and Engert, 2011). Gray always indicates medium gray (the center between black and white). The stimulus scene was a square window that was centered on the fish's head and spanned a field of total 60 × 60 mm.

Behavioral Triggered Average

We calculated the swimming vigor online as the standard deviation of a rolling buffer of 50 ms of the tail deflection angle. If vigor exceeded a given threshold, the visual stimulus was updated in closed-loop. Vigor was also used to determine bout starts and ends. Only bouts longer than 150 ms were included in the analysis, to avoid contamination with artifacts, struggles, and escapes. The random binary grating for each fish was also saved during the experiment. Thus, we could afterward determine the projected pattern before, on, and after bout onset (as shown in Figure 2B). We reduced the stimulus dimensionality to 1D, because the stimulus is only unique in one dimension (rostral to caudal), and stretched in the other (left to right). The history-dependent spatio-temporal stimulus has two dimensions: space (1D as described before) and time. We calculated the BTA by averaging all generated patterns across bouts, and then across individual fish:

$$ BTA \; = \; \frac{1}{N} \sum_i^N \frac{1}{n_i} \sum_j^{n_i} \vec{s_j} $$

where N is the number of fish, n_i the number of bout starts within a fish and $\vec{s_j}$ the spatio-temporal stimulus with a history of one to two seconds. To extract the grating directly from the camera image, we used a background image without presenting any stimulus. We focused on a part where the fish is not confounding the grating extraction and subtracted the background image from every camera image. We subsequently applied a threshold to this image to gain binary bars. The eyes of the fish was always centered on the camera chip for consistency across fish (XIMEA MG022RG-CM).

Nonlinearities were determined using the binned dot product of the BTA with the stimulus over time (Schwartz et al., 2006). The nonlinearity is the ratio between stimuli in each bin at bout triggered events and occurrences of all stimuli in that bin.

Behavioral Triggered Covariance Analysis

Similar to the spike triggered covariance, the behavioral triggered covariance is calculated using the following formula:

$$ BTC \; = \frac{1}{n_{bouts} - 1} \sum_i^n \left(\vec{s_i} \; - \; BTA \right) \left(\vec{s_i} \; - \; BTA \right)^T $$

We pooled all bouts from all fish together (N = 28230) and subtracted the overall mean of the whole dataset. We retrieved the eigenvalues and eigenvectors using singular-value decomposition of the BTC matrix using the scipy's implementation of the LAPACK SVD solver.

Binary Grating Edge Detection

We performed experiments as described before with different spatial frequencies showing alternating white and black, white and gray, and gray and black bars (see Figures S1E and S1F). We define spatial frequencies as such that we varied the rostro-caudal width of a periodic component (i.e., two adjacent bars) to 10, 30, 50 or 100 mm. We calculated the bout probability at a given luminance distribution by correlating the local stimulus area with a reference stimulus (light to dark to light luminance).

Luminance Experiments

We tested if pure luminance changes (either periodic, 1 s long white-black-white saw-tooth transitions as shown in Figure S1G, or as indicated in Figure S1H) are able to alter behavior or elicit swimming (Figures S1G and S1H, respectively). Luminance changes are either shown locally in a ± 5 mm window, in the periphery (the visual scenery, but not the ± 5 mm window, both Figure S1G) or in the whole visual scenery (Figure S1H).

Filter Replay

The filter as shown in Figure 3D was replayed to head-restrained larvae (the total six seconds in open-loop). As a control we shuffled the pixel values to disrupt the spatial correlation by keeping the same overall luminance. We also used the intensity profile on bout start of the filter, stretched this in 2D and then presented this in whole-field motion ensuring that filter replay and whole-field motion filter were probed the same amount of times. The stimuli are shown in Video S2.

Functional Imaging

Two-photon imaging was performed as described previously (Knogler et al., 2017). Briefly, nacre ($mitfa^{-/-}$) fish that express GCaMP6s pan-neuronally were embedded in 2% low melting point agarose and tail freed. Stimuli were presented using a Telefunken micro projector equipped with a red filter (Kodak Wratten no.29). Fish with no behavioral responses or significant drift were discarded. We presented the stimuli as shown in Figure 5A, namely a forward moving off edge, a whole-field luminance increase from black to maximum projector brightness, a sine grating moving forward, the whole-field filter moving forward and the reversed filter moving

backward. Each stimulus was presented for 9.7 s. After each set of stimuli, the imaging plane was moved 2 μm ventrally and the set of stimuli was repeated. Imaging data were sampled at approximately 3 Hz using a Ti:Sapphire laser tuned to 905 nm. We imaged a volume of approximately 468x468x240 μm per fish. Frames were aligned intra-plane and across planes. We then morphed the anatomy of individual fish to a reference brain (Knogler et al., 2017) using CMTK (Rohlfing and Maurer, 2003). The sampling coverage is shown in Figure S6. Behavior was recorded using a high-speed camera and custom-written software in Python, imaging data were acquired using custom-written software in LabVIEW.

Image Analysis

We used custom-written software in Python to correct for motion artifacts and to extract ROIs based on voxel-wise correlations (Portugues et al., 2014). We pooled the segmented ROIs across fish and clustered them into 20 groups using the scikit-learn implementation of k-means. Number of clusters was empirically determined. The anatomy of each fish was morphed to a reference brain yielding a transformation. We applied this transformation to the ROIs. To identify brain regions, we used the annotations provided by the Z-brain atlas (Randlett et al., 2015). First, we morphed the Tg(*elavl3*:GCaMP5g) confocal stack provided by the Z-brain atlas to our reference brain to compute a transformation. We used this transformation to morph each annotation map to our reference brain. With this, we have all experiments and all annotations in the same reference space. Then, we iterated over every voxel in our morphed cluster map and determined if this voxel is contained in any annotated map. Annotations with high relative coverage were considered being present in the cluster. For the swimming correlation map, we created a regressor mimicking an ideal fluorescence trace of a neuron coding linearly for swimming power using the swimming vigor (see above). To take into account the calcium dynamics, we convolved the regressor with the GCaMP6s kernel. ROIs that are correlated more than 0.8 were considered being swimming related ROIs.

Generalized Linear Model

We fitted a model similar to the one described in Haesemeyer et al. (2015). We fitted the following equation by minimizing the negative log likelihood. The input to the model is the grating history leading to a bout x_i. The model tries to predict the labels given the features, i.e., binary bout starts (0 no bout start, 1 bout start). We used 60 Hz as time basis.

$$\min_{\beta_0, \beta} \frac{1}{N} \sum_{i=1}^{N} L\left(y_i, \beta_0 + \beta^T x_i\right) + \lambda \left[0.5\left(1 - \alpha\right)\|\beta\|_2^2 + \alpha\|\beta\|_1\right]$$

We set alpha = 0, thus neglecting L1 regularization. The model with best performance as determined by ROC analysis had a $\lambda =$ 0.088. We used the pyglmnet package for fitting the data. Data were fitted on a fraction of total bouts and model performance was evaluated for the whole dataset of a given fish. To evaluate model performance we performed bootstrapping by shuffling the labels and determine true and false positive and negative rates. We shuffled 100 times and present the average with standard deviation across shuffles.

QUANTIFICATION AND STATISTICAL ANALYSIS

For all statistical tests, we used their implementation in Python. Number of samples are indicated in either the main text or the figure legend or both. Significance was tested using Student's t test with a significance level of 0.05, corrected by Bonferroni correction for multiple tests, if applicable. To determine if mean values of independent groups differ, we applied analysis of variance (ANOVA) with a significance level of 0.05. All error bars represent standard error of the mean (SEM) unless otherwise stated. Shaded error indicates either SEM or 5% to 95% percentile as stated in the panel caption.

DATA AND CODE AVAILABILITY

Custom-written code and acquired data are available upon request from the Lead Contact.